Time-resolved Fourier-transform infrared emission spectroscopy of Au in the 1800–4000-cm^{-1} region: Rydberg transitions

S. Civiš,[*] I. Matulková, and J. Cihelka

J. Heyrovský Institute of Physical Chemistry, Academy of Sciences of the Czech Republic, Dolejškova 3, CZ-18223 Prague 8, Czech Republic

K. Kawaguchi

Faculty of Science, Okayama University, Tsushima-naka, Okayama 700-8530, Japan

V. E. Chernov and E. Yu. Buslov

Voronezh State University, RV-394693 Voronezh, Russia

Time-resolved Fourier-transform infrared spectroscopy was applied for observations of the emission arising after irradiation of a Au target with a pulsed nanosecond ArF ($\lambda = 193$ nm) laser. A high-repetition-rate laser (1.0 kHz) with an output energy of 15 mJ was focused on a rotating metal target inside a vacuum chamber (average pressure 10^{-2} Torr). The infrared emission spectra were observed in the 1800–4000 cm^{-1} spectral region with a time profile showing maximum emission intensity in 9–11 μs after a laser shot. Seven prominent lines are reported; most of them are identified as being due to transitions between low Rydberg nl states of Au with $n = 5$–10 and $l = 0$–3. An alternative identification ($6f_{5/2} \rightarrow 7d_{3/2}$) is given for the 2518.489 cm^{-1} line previously classified as $8d_{5/2} \rightarrow 5f_{5/2}$. On the basis of the measured lines, three f levels of the Au atom are reported and revised values are given for six other levels.

I. INTRODUCTION

The chemistry of Au has been intensively developed in recent years [1]. Such interest is due to the physical and chemical properties of certain Au compounds and clusters or to the possibility of forming new nanostructures based on Au, with applications in catalysis, materials science, and medicine [2]. Although the infrared (IR) spectra of Au clusters are being actively studied, the atomic Au IR lines are not completely known. Indeed, while the Au spectrum was studied in various spectral domains for several decades [3–9], to our knowledge only one experimental work [7] concerning the IR range was reported.

The energy levels of Au can be subdivided into several groups. One group of levels is formed by the excitation of the outer $6s$ electron to nl states beyond the closed-shell ($1s^2 2s^2, \ldots, 5d^{10}$) core. This group is similar to the level system of alkali-metal atoms and is well described in terms of the Russell-Saunders (LS) coupling scheme. Since the closed-shell ($5d^{10}$) configuration can form only the ^1S term, all the terms ($5d^{10})nl_j$ of the first group of Au levels can be classified according to the orbital (l) and total ($j = l \pm \frac{1}{2}$) angular momentum of the outer electron as well as according to its principal quantum number n. The remaining groups of levels are formed by the excitation of one $5d$ electron from the $5d^{10}$ core to the configurations ($5d^9 6s)nl_j$. A further subdivision of the levels belonging to these groups can be made according to the angular momentum J_s of the $5d^9$ subshell and to the ($5d^9 6s$) core momentum $J_c = J_s \pm \frac{1}{2}$. The LS coupling is inadequate for such states and they are described by a jj-like coupling scheme $[(5d^9_{J_s}6s)_{J_c} nl_j]_{J_{\text{total}}}$.

The spectrum of neutral Au has been studied for several decades. Platt and Sawyer [3] measured the Au spectrum in a hollow cathode discharge in He. They classified 318 lines in the 150–1010 nm range and reported energy values for 46 even and 17 odd Au levels.

Ehrhardt and Davis [4] recorded the hollow-cathode spectrum of Au from 260 to 960 nm and classified 110 lines, giving values for 17 odd and 35 even levels (among which 10 autoionized levels are reported for Au).

The high-dispersion absorption spectrum of Au I was photographed by Brown and Ginter [5] in the 130–190 nm region. They present identification for 78 lines providing energies of the same number of levels since all the observed lines were due to transitions from the ground ($5d^{10})6s_{1/2}$ term. Among these levels, Rydberg states ($5d^{10})np_{1/2,3/2}$ are reported up to $n = 42$ from which the Au ionization limit was evaluated to 74408.88 ± 0.17 cm^{-1}.

The analysis of the absorption spectrum of Au above the first ionization limit was extended by Jannitti *et al.* [6], who observed 130 lines in atomic vapors produced with an induction heated furnace and flash-pyrolysis in the 96–210 nm range. Most of the observed lines were classified in 15 series corresponding to transitions $5d^{10}6s$–$5d^9 6snp, nf$ and converging to the first four limits above the first ionization limit. Reference [6] contains a useful diagram of Au energy levels including a number of autoionized levels.

High-resolution (with the resolved hyperfine structure of some lines) Fourier-transform (FT) spectra of a hollow Au cathode in the 1–5.3 μm region were performed by George, Grays, and Engleman [7] who recorded 29 lines and improved the energy values for eight levels. However, they did not report some prominent lines, which are observed in the present work. Moreover, their classification of one prominent line is not supported by our measurements (see Results and Discussion).

_____
[*]civis@jh-inst.cas.cz

Using resonance excitation followed by electric field ionization, Ding *et al.* [8] studied about 38 high Rydberg $(5d^{10})nd_{3/2}$ and $(5d^{10})ns_{1/2}$ levels of the Au atom. The fitted thresholds for these series gave, for the first ionization, a limit of 74409.8(3) cm^{-1} and 74410.0(2) cm^{-1}, respectively.

Dyubko *et al.* [9] measured energies of laser-excited Au in Rydberg $(5d^{10})ns_{1/2}$, $np_{1/2,3/2}$, and $nd_{3/2}$ states (*n* from 25 to 38) by means of millimeter-wave spectroscopy in the 80–300 GHz range. They obtained an improved value of 74409.11 ± 0.03 cm^{-1} for the first ionization potential for Au.

Although the spectra of the Au atom were studied in various frequency ranges, our study points to the existence of spectral lines, which have not yet been observed. In the present work we classify several lines of the Au atom in the 3–5 μm IR range.

While the visible spectral lines are due to the transitions involving the ground and low-excited states, the IR lines in atoms correspond to the transitions between highly excited (Rydberg) levels. To investigate the Rydberg states with more or less known energies (e.g., as it was done for Au in Refs. [8,9]), these electronic levels are excited by tunable lasers with frequencies varying within a comparatively narrow range. Such a complicated experiment may require two excitation steps using different lasers for each step. However, if the exact positions of the levels under study are not known, it is more reasonable to work with a plasma where all these levels are populated.

Such a technique, known as laser-induced breakdown spectroscopy (LIBS), consists of analyzing the spectrum emitted from the plasma created on the sample surface by low-fluence (typically 10 J/cm^2) laser pulses. LIPS has many practical advantages over the conventional methods of chemical analysis of elements and is consequently being considered for a growing number of applications [10–13].

The properties of the observed plasma plumes obtained by the ablation of different materials can eventually reflect the superposition of the ensemble of various processes [12–17]. The population of Rydberg states responsible for IR emission lines is governed mainly by collisional processes. The electron-ion collision inside the plume can create excited ions. The electron-ion collision in the presence of a third body can result in their recombination, leading to the formation of atoms in highly excited Rydberg states [18]. A radiative cascade of these Rydberg states is then observed as the emission of the ablation plume. The investigation of such an emission is complicated by nonequilibrium and nonstationary conditions of the plasma for the excited states [13], so the available information on population dynamics for these states [19] is scarce. As an example of such data, we report temporal evolution dynamics for each IR atomic line of the recorded atomic Au spectrum.

II. EXPERIMENTAL

A. Time-resolved Fourier-transform infrared spectroscopy

Time-resolved FT spectroscopy (TR-FTS) is a wide-spectrum technique used for studying the dynamics of chemical reactions or the dynamic properties of molecules, radicals, and ions in liquid, gas, and solid states. The main advantage of TR-FTS lies in obtaining spectra in wide wave number

intervals. The speed of data acquisition is limited by the duration of the acquisition process and by the bandwidth of the detector. There are basically two methods of obtaining the time-resolved spectra: the continuous scan and the noncontinuous, step scan [20,21].

The continuous scan is best used when the duration of the observed phenomenon is longer than the time needed for carrying out one scan, that is, for obtaining an interferogram up to the maximum path difference (Rapid and ultrarapid scanning FT). Time-shifted individual scans provide a sequence of interferograms from which a conventional spectrum can be calculated. When using the rapid-scanning and short-distance mirror traversing, a time resolution from 1000 s to 1 ms can be reached.

A special approach to the time-resolved spectra of phenomena lasting from milliseconds to microseconds is the synchronous scanning FT technique [22]. This method, as well as the methods mentioned in the following, requires the possibility of initiating the reaction in a pulse mode, for example, using a laser, electric discharge, electron bombardment, a UV discharge lamp, and so on [23].

Continuously scanning spectrometers have been applied for time-resolved spectroscopy by several teams following the first report by Mantz [24]. Berg and Sloan [25] developed a compact data acquisition system for submicrosecond time-resolved FTS. Nakanaga *et al.* [26] applied a pulse discharge system to a continuously scanning interferometer without any modification of the system's software. The pulsed discharge was triggered by a HeNe laser fringe signal with an appropriate delay time. The system was applied to the measurement of the time profiles of a vibrational-rotation absorption spectrum of discharged CO. Recently, Kawaguchi [22] reviewed the methods of time-resolved Fourier-transform infrared spectroscopy and its application to pulsed discharges and demonstrated the technique of FTS using a high-resolution Bruker IFS 120 HR supported by a microcontroller SX on He$_2$, ArH, and ArH$^+$ spectra. The same system was used for studying the products of Nd: YLF of laser ablation products [27].

The continuous scanning principle was the basis for data acquisition by a modified (Bruker IFS 120) spectrometer in our laboratory at the J. Heyrovský Institute of Physical Chemistry and a similarly modified spectrometer was used in Okayama (Japan).

B. Interleaved sampling 1/*n*

In the case of the measurement of time-resolved spectra in combination with a laser whose maximum repetition rate is slower than the HeNe fringe frequency, there is no possibility of sampling at each individual trigger point of the HeNe laser.

The lowest scanning speed of the interferometer is limited to the HeNe laser fringe frequency of about 3 kHz. However, by utilizing the undersampling condition, sampling several times more slowly becomes possible. Figure 1 shows the clock pattern for sampling in the present experiments where triggers for the pulse event and for the sampling are produced with a period of 1/*n* times the HeNe laser fringe frequency. Complete interferograms are then obtained with *n* scans if the trigger point is changed for each scan. The time sequence shown in Fig. 1 corresponds to the case of *n* = 3.
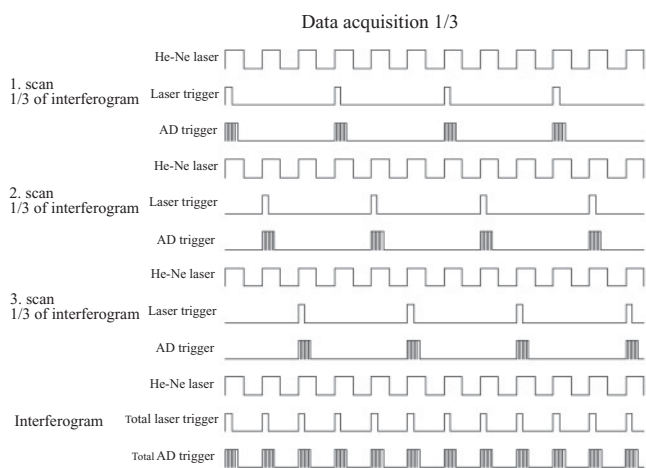
FIG. 1. Timing diagram for the interleaved sampling. During the scan, the laser pulse and the analog–digital (AD) trigger sampling are induced with a rate of $1/n$ times that of the HeNe laser fringe frequency. The complete interferograms are obtained after n scans.

The maximum frequency of the used ArF laser is 1 kHz. The laser pulse is therefore repeated every 1000 μs. The minimum speed of the interferometer mirror is 3 kHz; the digital signal produced by the HeNe laser is then repeated every 333.33 μs. To obtain data in the maximum density (i.e., for every path difference defined by the HeNe laser) the complete record is taken over three scans (for the mirror speed 3 kHz and laser repetition frequency 1 kHz). The complete set of the time-resolved spectra (one complete interferogram) is acquired by three time-shifted scans.

C. Synchronous triggering and data sampling

FT data are taken at the zero-crossing points of the HeNe laser fringe signals, while the wavelength of the HeNe laser is used for the measurement of path differences. The data are sampled at time intervals that correspond to a mirror movement of either one wavelength or half a wavelength, depending on the frequency range of the measurements (8000 or 16000 cm^{-1}). Time-resolved spectra are obtained by collecting data at various points between the zero-crossings and calculating the FT for each such point. This system was employed using a field programmable gate array processor (FPGA). The main role of the FPGA processor in our experiment was to create a discharge or laser pulse and AD trigger signals (the signal for data collection from the detector) synchronously with the HeNe laser fringe signals from the spectrometer. The FPGA processor also controls the data transmission from the digital input board to the PC.

Figure 1 depicts the timing chart (clock pattern) produced by the FPGA for the laser-pulse ablation method. The scan signal and HeNe laser fringe signals are supplied by the Bruker 120 HR spectrometer and used as the system time standard. A discharge trigger pulse is produced at a width that is preset by the FPGA. AD triggers are also produced by the FPGA with a time offset value between the beginning of the laser pulse and the interval between pulses. In the present experiments we used a 60 μs offset and interval values covering 30 μs when 30 AD

triggers were supplied. A series of data signals corresponding to the AD triggers are stored and Fourier transformed. The maximum number of spectra taken by this method is 64. The time resolution is about 1 μs, which is limited by the bandwidth of the detector amplifier.

The present system collects 64 times more data in comparison to the original Bruker system. This is possible because of rapid development in the field of PCs, their memory size, and the writing speed of the hard disk.

In the case of our current data collection program, we are able to store 64 interferograms in a single scan when the resolution is up to 0.03 cm^{-1}. For resolutions higher than 0.03 cm^{-1}, 30 time-resolved data are recorded simultaneously, which means the number of time-resolved data points can be varied according to the type of experiment and the memory capacity.

The resolution used in the present work is optimized according to the data acquisition process and to the excimer laser's limitation in number of pulses. The highest resolution of our system is limited to 0.0035 cm^{-1}.

D. The experimental setup

The time resolution FTIR spectra were measured using the modified Bruker IFS 120 HR spectrometer (modified for the time-resolution scan of emission data) in a spectral range of 1800–4000 cm^{-1} using a CaF_2 beam splitter and an InSb detector. The aperture size was 4 mm, the preamplifier gain was 3. The spectra were measured at a resolution of 0.1 cm^{-1} with an mid-IR filter (number of scans from one to ten, zero filling two, and trapezoid apodization function).

The Bruker system was equipped with an analog-digital converter (ADC 4322: Analogic, USA), which was connected to a PC containing a programmable control processor of FPGA, (ACEX 1K: Altera, USA) set up at a frequency of 33 MHz, and a digital input board PCI (2172C: Interface, Japan). The data collection process and synchronization with the laser were controlled by the FPGA processor programed by QUARTUS II 7.1, Altera. The computer programs for data acquisition and fast FT transformation and displaying of the data were written in C^{++} language.

Time-resolved FTIR spectroscopy was applied for observations of the emission arising after the irradiation of metals with a pulsed nanosecond ArF ($\lambda = 193$ nm) laser. A high-repetition-rate ArF laser ExciStar S-Industrial V2.0 1000 (193 nm, laser pulse width 12 ns, frequency 1 kHz) with 15 mJ output power was focused on a rotating and linearly traversing Au target inside a vacuum chamber (average pressure 10^{-2} Torr). The IR emission (axial distance from the target 10 mm) was focused into the spectrometer using a CaF_2 (100 mm) lens (see Fig. 2). The time profiles of the emission lines show the maximum emission intensity at 9–11 μs after the laser shot (see Fig. 4).

For data sampling we used the so-called 1/3 sampling, where the scanner rate was set to produce a 3 kHz HeNe laser interference signal, the ArF laser oscillation was triggered and 30 sets of time-resolved data were recorded with a preset time interval of 1 μs. Three scans were needed for a complete interferogram and only five sets of scans were coadded to improve the signal-to-noise ratio. The acquired spectra were
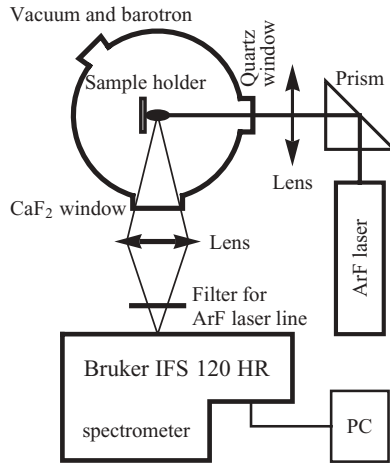
FIG. 2. Experimental set-up of the metal emission measurement.

FIG. 3. Some parts of the observed IR emission spectra of Au. The 2743.358 cm^{-1} and 2747.567 cm^{-1} values in Table I are given to the centers of gravity of the hyperfine patterns clearly seen in the second graph as double peaks.

post-zerofilled in the Bruker OPUS software package [28] and subsequently corrected by subtracting the blackbody background spectrum. The wave numbers, linewidths, and their intensities were then obtained using the peak picking method (using OPUS).

III. RESULTS AND DISCUSSION

The observed IR emission spectra of the Au atom are presented in Fig. 3 at 10 μs after the laser shot, when the time profile of the emission intensity is maximum for all the observed lines.

As compared to Ref. [7], we observed several strong additional Au lines in the 1800–4000 cm^{-1} domain. The most prominent IR lines observed for Au are listed in Table I. Their halfwidths at halfmaxima (HWHM) are calculated from fitting to the Voigt profile, but under our conditions this profile does not differ much from the Lorentzian shape because the Doppler broadening can usually be neglected as compared to Stark
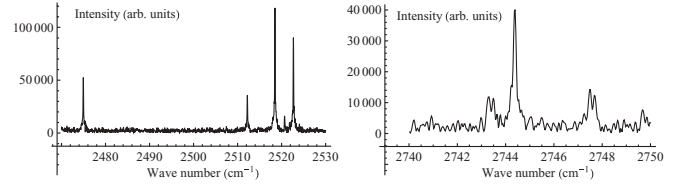
broadening, which is well described by a Lorentzian profile [29,30]. Indeed, for a line with the frequency ω_0, its Doppler broadening is estimated as $\Delta\omega_D = (2\omega_0/c)\sqrt{2k_B T/m}$ [31] where c is speed of light, m is the atom mass, and k_B is the Boltzmann constant. For the temperatures $T \simeq 4000$ K and $\omega_0 \simeq 3000$ cm^{-1} we obtain $\Delta\omega_D \simeq 0.01$ cm^{-1}. The natural broadening can be estimated from the radiative lifetimes of Au atomic states. For example, the radiative lifetimes of $8p$ and $9p$ states are 20–70 ns [32] and give the natural linewidth estimation of an order of 10^{-3} cm^{-1}.

The recorded time profiles allow us to measure the relaxation time of the individual atomic transitions. Such information can be helpful for diagnostics of the electronic state populations of neutral atoms and ions in plumes formed by pulsed laser ablation [33]; however, there are few reports of studies of such population dynamics [19]. The recorded spectral lines are measured in a vacuum, that is, without the presence of any buffer gases. So we suppose that their relaxation should describe the population of individual Rydberg levels of Au atoms without the interference with other substances. The depopulation in these levels is governed by complex collisional processes inside the plasma plume (depending on the plasma temperature and density, laser frequency, and pulse energy, etc.), which are important for explaining the time profiles.

TABLE I. Experimental Au lines and their identification. The decay time, τ, was calculated by exponential fitting of the measured time profiles of the corresponding lines.

Wave number (cm^{-1})	Intensity (arb. units)	HWHM (cm^{-1})	Decay time (μs)	Identification
2156.484	12679	0.098	5.24 ± 1.7[a]	$8f_{7/2} \rightarrow 8d_{5/2}$
2193.030	38690	0.12	6.56 ± 0.61	$8s_{1/2} \rightarrow 8p_{1/2}$
2428.358	8024	0.39	6.36 ± 1.4[a]	$12s_{1/2} \rightarrow 9p_{3/2}$
2474.954	53951	0.13	5.25 ± 0.21	$7d_{5/2} \rightarrow 6f_{7/2}$
2512.219	36631	0.14	5.73 ± 0.25	$9p_{1/2} \rightarrow 10d_{3/2}$
2518.489	121588	0.13	5.56 ± 0.22	$7d_{3/2} \rightarrow 6f_{5/2}$
2520.684	16574	0.16	6.83 ± 0.58	$8p_{3/2} \rightarrow 8d_{5/2}$
2522.683	91622	0.13	5.70 ± 0.36	$5f_{\frac{7}{2}} \rightarrow 8d_{5/2}$
2743.370	8780	0.39	5.41 ± 1.2[a]	?
2744.380	41786	0.12	5.96 ± 0.68	$8s_{1/2} \rightarrow 8p_{3/2}$
2747.567	10249	0.13	8.52 ± 2.6[a]	$12s_{1/2} \rightarrow 9p_{1/2}$
2749.6	6453	0.27	5.51 ± 1.8[a]	$23p_{1/2,3/2} \rightarrow 9d_{3/2}$
3187.811	13199	0.093	6.03 ± 0.91[a]	$(5d^96s)6p_{3/2} \rightarrow 6d_{5/2}$
3828.96	9540	0.14	5.47 ± 2.0[a]	$7f_{7/2} \rightarrow 7d_{5/2}$
3862.41	9370	0.13	2.98 ± 1.1[a]	$9d_{3/2} \rightarrow 5f_{5/2}$
3866.606	7738	0.11	6.84 ± 0.83[a]	$9d_{3/2} \rightarrow 8p_{3/2}$

[a]Time profile demonstrates significant deviation from the exponential decay; τ values are roughly approximate.
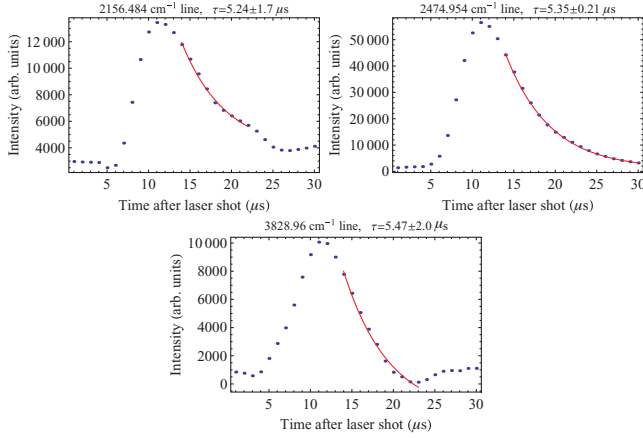
FIG. 4. (Color online) The time profiles of some observed lines (dots) and their fit with exponential decay (solid curves).

Some examples of the measured time profiles are given in Fig. 4. The time decay of most of the strong lines is well described by exponential fitting, except the 2156.484 cm^{-1} line, which demonstrates a nonconstant decay rate during the 30 μs after the laser shot. Some weaker lines demonstrate such behavior more clearly, their decay is not exponential (and is even nonmonotonic), so their τ values are estimated in Table I in a rough approximation.

Note that the decay times $\tau \simeq$ 1–10 μs given in Table I cannot be justified as the radiative lifetimes of the isolated Au atom levels, which are at least two orders shorter [32]. The time dynamics shown in Fig. 4 should be governed by processes of cascades repopulating emitting levels due to their collisional deexcitation. The problem is complicated by the breaking of local thermal equilibrium conditions for upper atomic levels and long delay times after the laser pulse [13]. Such complex population kinetics of the atomic Au states in the ablation plasma results, in particular, in the noted nonexponential decay of the line intensities. Its explanation is beyond the scope of the present article since the establishment of the relationships between the populations of electronic levels and the main plasma characteristics in the absence of complete or local equilibrium is a fairly difficult problem of plasma theory [31].

We consider most of the observed lines to be due to transitions between the Rydberg $n = 5$–10 states of the valence electron outside the closed-shell $5d^{10}$ core. Our identification procedure uses the literature data [3–7] and for each identified $nlj \rightarrow n'l'j'$ line we attempted to find all the lines corresponding to all allowed transitions between nl and $n'l'$ multiplets. This classification took into account the relative intensities of the transitions in an isolated atom, which are determined by the values of the dipole transition matrix elements between the valence electron states. These matrix elements were calculated using the Fues model potential [34]. This method proved its efficiency for the calculation of atomic and molecular matrix elements of single [35] and higher [36] orders.

In this approximation the normalized wave function of the valence nl_j electron has a Coulomb-like form and can be expressed in terms of Whittaker functions, Gaussian

hypergeometric functions, or Laguerre polynomials [37]:

$$\langle r|nljm \rangle = R_{nlj}(r) \sum_{\mu\sigma} \langle l\mu\tfrac{1}{2}\sigma \,|\, jm \rangle Y_{l\mu}(\hat{r}) \chi_{\frac{1}{2}\sigma}$$

$$= \frac{2Z^{3/2}}{n^{*2}} \frac{N}{\Gamma(2\tilde{l}+2)} \frac{1}{x} M_{n^*,\tilde{l}+\frac{1}{2}}(x)$$

$$= \frac{2Z^{3/2}}{n^{*2}} \frac{N}{\Gamma(2\tilde{l}+2)} x^{\tilde{l}} e^{-x/2} \,_1F_1(-n_r, 2\tilde{l}+2; x)$$

$$= \frac{2Z^{3/2}}{n^{*2}} \frac{1}{N} x^{\tilde{l}} e^{-x/2} L_{n_r}^{2\tilde{l}+1}(x);$$

$$N = \sqrt{\frac{\Gamma(n_r + 2\tilde{l} + 2)}{n_r!}}, \qquad x = \frac{2Zr}{n^*}, \qquad (1)$$

where $\Gamma(\cdot)$ is the Gamma function. The effective principal quantum number n^* is connected to the energy level $E(nl_j)$ and quantum defect μ_{lj} via the Rydberg formula

$$E(nl_j) = V_i - \frac{Z^2}{2n^{*2}} = V_i - \frac{Z^2}{2(n - \mu_{lj})^2}, \qquad (2)$$

where V_i stands for ionization potential and the $(5d^{10})$ core's charge $Z = 1$. The noninteger parameter $\tilde{l}$ accounts for the non-Coulombic potential of the core and it is connected to the principal quantum number in the following way:

$$n^* = n_r + \tilde{l} + 1. \qquad (3)$$

The integer radial quantum number n_r is equal to the number of nodes of the radial wave function $R(r)$; it is assumed that $n_r = 0$ for the first (lowest) level of a series with a given l (s, p, d, $etc.$) and n_r increases for each consequent level of the series. A possible exception can occur for the ground s state, for which $n_r = 0$ is often used in model potential calculations [38]. Thus, for the Au atom, this number was determined as

$$n_r = \begin{cases} \max\{1, n - 6\} & \text{for} \quad s, p, d \text{ states } (n \geqslant 6); \\ n_r = n - 5 & \text{for} \quad f \text{ states } (n \geqslant 5). \end{cases} \qquad (4)$$

Note that all the quantum numbers $(n^*, n_r, \tilde{l})$ occuring in Eq. (1) are dependent on the "spectroscopic" numbers (n, l, j) via Eqs. (2), (3), and (4). The dependence on j occurs because of different quantum defect μ_{lj} values for the different fine-structure components. In essence, the model potential approach is close to the single-channel quantum defect theory, which is also a simple and quantitatively adequate method for the calculation of first-order [35] and second-order [39] matrix elements in atoms and molecules. For other methods of the calcualtion of matrix elements for transitions between Rydberg states, see Ref. [40].

To evaluate the relative strengths of the observed lines, we calculate the matrix elements [41]

$$S(nlj; n'l'j') = (2j+1)(2j'+1)\max\{l, l'\}$$

$$\times \left[W\left(ljl'j'; \tfrac{1}{2}1\right) \int_0^\infty r^3 R_{nlj} R_{n'l'j'} dr \right]^2, \qquad (5)$$

where W are the Racah coefficients.

The results of our calculation presented in Table II demonstrate satisfactory agreement with relativistic *ab initio* calculations [42]. Some discrepancies (factors of $\sim$1.4)

TABLE II. Dipole transition matrix elements $\sqrt{S}$ [see Eq. (5)] for transitions between $(5d^{10})nl_j$ levels of Au.

Transition	$Z^{(2)}$ MBPT [42]	This work
$6s_{1/2} \rightarrow 6p_{1/2}$	2.114	2.062
$6s_{1/2} \rightarrow 6p_{3/2}$	2.972	2.274
$6p_{1/2} \rightarrow 6d_{3/2}$	4.556	3.556
$6p_{3/2} \rightarrow 6d_{3/2}$	2.447	3.441
$6p_{3/2} \rightarrow 6d_{5/2}$	7.286	10.30
$6p_{1/2} \rightarrow 7s_{1/2}$	3.113	2.402
$6p_{3/2} \rightarrow 7s_{1/2}$	5.355	7.386
$6s_{1/2} \rightarrow 7p_{1/2}$	0.163	0.308
$6s_{1/2} \rightarrow 7p_{3/2}$	0.479	0.554
$7s_{1/2} \rightarrow 7p_{1/2}$	7.137	6.526
$6d_{3/2} \rightarrow 7p_{1/2}$	12.275	11.520
$7s_{1/2} \rightarrow 7p_{3/2}$	9.467	8.939
$6d_{3/2} \rightarrow 7p_{3/2}$	5.388	5.170
$6d_{5/2} \rightarrow 7p_{3/2}$	16.319	15.596
$8d_{5/2} \rightarrow 5f_{7/2}$	1.853	2.854
$8d_{5/2} \rightarrow 5f_{5/2}$	0.415	0.639
$8d_{3/2} \rightarrow 5f_{5/2}$	1.706	2.710
$7d_{5/2} \rightarrow 6f_{7/2}$	29.04	26.09
$7d_{5/2} \rightarrow 6f_{5/2}$	6.496	5.828
$7d_{3/2} \rightarrow 6f_{5/2}$	23.89	21.38
$8d_{5/2} \rightarrow 8p_{3/2}$	18.42	12.99
$8p_{3/2} \rightarrow 8s_{1/2}$	17.49	16.89
$8p_{1/2} \rightarrow 8s_{1/2}$	13.38	12.89
$10d_{3/2} \rightarrow 9p_{1/2}$	6.283	4.376
$10d_{3/2} \rightarrow 9p_{3/2}$	3.307	2.999
$12s_{1/2} \rightarrow 9p_{1/2}$		1.947
$12s_{1/2} \rightarrow 9p_{3/2}$		1.695
$23s_{1/2} \rightarrow 9p_{1/2}$		0.212
$23s_{1/2} \rightarrow 9p_{3/2}$		0.156

should not be considered as striking. The different models in relativistic *ab initio* calculations [42] display the same order of discrepancies in the dipole matrix elements, not to mention the calculated energy values, which disagree with experimental values by several tens or even hundreds of cm^{-1}. Although semiphenomenological, our Fues model-potential calculations are known to be adequate especially for higher-excited states for which the relativistic *ab initio* calculations are not available [42].

The reduced matrix elements presented in Table IV of Ref. [42] are, in fact, equal to the square root of $S(nlj; n'l'j')$ values (5). In equilibrium at low temperatures, the intensities of $nlj \rightarrow n'l'j'$ transition lines are proportional to $S(nlj; n'l'j')$. Under real experimental conditions this proportionality may break down due to self-absorption and nonequilibrium population dynamics in the plasma plume, but the qualitative picture of the relative intensities of different lines should be adequately described by S values.

In particular, our account for the relative intensities shows that the most prominent 2518.489 cm^{-1} line is hardly likely to be due to the $8d_{5/2} \rightarrow 5f_{5/2}$ transition as is claimed in Ref. [7]. Indeed, first, owing to the properties of Racah coefficients, one can clearly see that the $8d_{5/2} \rightarrow 5f_{7/2}$ transition should be 20 times more intense than the $8d_{5/2} \rightarrow 5f_{5/2}$ transition in the nonrelativistic approximation. Second, the $7d_{3/2} \rightarrow 6f_{5/2}$

transition has almost the same frequency. Indeed, due to very small quantum defects for f states we can assume for the $6f_{5/2}$ state the same quantum defect as for the $5f_{5/2}$ state, which, in turn, can be taken from the experimental energy value $E(5f_{5/2})$ of this state [3]. Then, according to the Rydberg formula (2), we have $E(6f_{5/2}) = 69988.301$ cm^{-1}. Subtracting from this value the experimental [4] value $E(7d_{3/2}) = 67469.683$ cm^{-1}, we obtain 2518.618 cm^{-1}. According to our evaluation, $6f_{5/2} \rightarrow 7d_{3/2}$ should be the most prominent of the considered transitions. Therefore, it is the transition we consider to be responsible for the strongest 2518.489 cm^{-1} line. The observed value for the 3187.811 cm^{-1} line coincides with that reported in Ref. [7]; this line involves a $5d^9$ core state. We were not able to classify the weak 2743.38 cm^{-1} line using only the states lying below the first Au ionization limit. Although the energy difference between the autoionizing $[(5d_{5/2}^9 6s)_2 7p_{1/2}]_{3/2}$ state ($E = 76742.4$ cm^{-1}) [6] and the Rydberg $21s_{1/2}$ state ($E = 73999.4$ cm^{-1}) [43] is close to 2743 cm^{-1}, the width of this line is not much bigger than that of the other lines, therefore it can hardly be explained by a transition to an autoionizing state whose width should be greater by some orders of magnitude.

The revised values of some Rydberg $(5d^{10})nl_j$ terms are presented in Table II. We consider the $7d_{3/2,5/2}$ and $8d_{5/2}$ terms as reference terms since their energies reported in different sources are almost identical. In the $9p_{1/2,3/2}$ doublet, one level was considered a reference and the other was to be given a revised value; both variants are presented in Table III. Depending on these variants, the revised value for one of two other levels, $10d_{3/2}$ and $12s_{1/2}$, differs by approximately 2.6 cm^{-1} from that reported [4]. The discrepancy for other levels in Table III is less than 0.5 cm^{-1}. The $8p_{1/2}$ term in our identification is closer to the older [5] than to the more recent [7] results. While the authors of Ref. [5] justify their rejection of the previous [3] assignments for the $8p$ levels, it is striking that the authors of Ref. [7] slightly revise the older value 66605 cm^{-1} [3] without any reference to the more

TABLE III. Revised values of some levels of Au.

Level (cm^{-1})	Term	Note
67485.292	$5f_{7/2}$	67485.3 [3]
67491.487	$5f_{5/2}$	67490.0 [3], 67489.276 [7]
69985.559	$6f_{7/2}$	This work
69988.172	$6f_{5/2}$	This work
71339.569	$7f_{7/2}$	This work
72164.459	$8f_{7/2}$	Reported from weak 3828.9 cm^{-1} line
64742.911	$8s_{1/2}$	64742.4 [3], 64742.896 [4]
67487.291	$8p_{3/2}$	67487.11 [5]
66935.941	$8p_{1/2}$	66935.76 [5], 66604.87 [7], 66605.3 [3]
69650.681[a]	$9p_{1/2}$	69648.28 [5]
69967.489[b]	$9p_{3/2}$	69969.89 [5]
71353.897	$9d_{3/2}$	71354.4 [3], 71354.953 [4]
72162.900[a]	$10d_{3/2}$	72163.346 [4], 72163.8 [3]
72160.499[b]	$10d_{3/2}$	72163.346 [4], 72163.8 [3]
72398.248[a]	$12s_{1/2}$	72395.9 [3]
72395.847[b]	$12s_{1/2}$	72395.9 [3]

[a]Reference value 69969.89 cm^{-1} [5] used for $9p_{3/2}$ level.
[b]Reference value 69648.28 cm^{-1} [5] used for $9p_{1/2}$ level.

recent value [5], which disagrees by as much as 331 cm^{-1}. Nevertheless, our revised value supports the value currently adopted in atomic level databases [43]. The $nf_{7/2}$ terms with $n = 6$–8 are reported; the quantum defect of the $8f_{7/2}$ state demonstrates a deviation from the quantum defects of the $nf_{7/2}$ terms with $n = 5$–7. We consider this peculiarity to be due to perturbation of nf terms by nd Rydberg states.

IV. CONCLUSION

The TR FTIR emission spectrum of Au was recorded in the 1800–3600 cm^{-1} spectral region. The emission arises in the ablation of a Au target by laser radiation of a pulsed nanosecond ArF ($\lambda = 193$ nm) laser. This study extends the knowledge of Au emission IR spectra by classifying several lines due to transitions between low Rydberg $(5d^{10})ns$, p, d, f states with n between 5 and 10. The time profiles of the lines show maximum emission intensity at 9–11 μs after the laser shot. Based on the relative values for the dipole matrix elements, we correct the previous identification for the 2518.489 cm^{-1} line and present energy values of three f states.

[1] P. Pyykkö, Angew. Chem. Int. Ed.**43**, 4412 (2004); Inorg. Chim. Acta **358**, 4113 (2005); Chem. Soc. Rev. **37**, 1967 (2008).

[2] R. A. Sperling, P. R. Gil, F. Zhang, M. Zanella, and W. J. Parak, Chem. Soc. Rev. **37**, 1896 (2008).

[3] J. R. Platt and R. A. Sawler, Phys. Rev. **60**, 866 (1941).

[4] J. C. Ehrhardt and S. P. Davis, J. Opt. Soc. Am. **61**, 1342 (1971).

[5] C. M. Brown and M. L. Ginter, J. Opt. Soc. Am. **68**, 243 (1978).

[6] E. Jannitti *et al.*, Phys. Scr. **20**, 156 (1979).

[7] S. George, A. Grays, and R. Engleman, J. Opt. Soc. Am. B **5**, 1500 (1988).

[8] G. J. Ding *et al.*, J. Phys. B **22**, 1555 (1989).

[9] S. F. Dyubko *et al.*, J. Phys. B **38**, 1107 (2005).

[10] W. B. Lee, J. Wu, Y. L. Lee, and J. Sneddon, Appl. Spectrosc. Rev. **39**, 27 (2004).

[11] D. Babánková, S. Civiš, and L. Juha, Prog. Quantum Electron. **30**, 75 (2006).

[12] C. Pasquini, J. Cortez, L. M. C. Silva, and F. B. Gonzaga, J. Braz. Chem. Soc. **18**, 463 (2007).

[13] C. Aragón and J. Aguiliera, Specrochim. Acta B **63**, 893 (2008).

[14] F. Claeyssens, S. J. Henley, and M. N. R. Ashfold, J. Appl. Phys. **94**, 2203 (2003).

[15] A. Miotello and R. Kelly, Appl. Phys. **69** [Suppl.], S67 (1999).

[16] H. G. Rubahn, in *Laser Application in Surface Science and Technology* (Wiley, New York, 1999), p. 219.

[17] A. Vertes, R. W. Dreyfus, and D. E. Platt, IBM J. Res. Dev. **38**, 3 (1994).

[18] F. Claeyssens, R. J. Lade, K. N. Rosser, and M. N. R. Ashfold, J. Appl. Phys. **89**, 697 (2001).

[19] M. Rossa, C. A. Rinaldi, and J. C. Ferrero, J. Appl. Phys. **105**, 063306 (2009).

[20] G. D. Smith and R. A. Palmer, in *Handbook of Vibrational Spectroscopy*, edited by J. M. Chalmers and P. R. Griffiths (Wiley, Chichester, 2002), Vol. 1, pp. 625–640.

[21] C. Rödig and F. Siebert, in *Handbook of Vibrational Spectroscopy*, edited by J. M. Chalmers and P. R. Griffiths (Wiley, Chichester, 2002), Vol. 1, pp. 641–654.

[22] K. Kawaguchi, Y. Hama, and S. Nishida, J. Mol. Spectrosc. **232**, 1 (2005).

[23] S. Civiš, P. Kubát, S. Nishida, and K. Kawaguchi, Chem. Phys. Lett. **418**, 448 (2006).

[24] A. W. Mantz, Appl. Spectrosc. **30**, 459 (1976).

[25] P. A. Berg and J. J. Sloan, Rev. Sci. Instrum. **64**, 2508 (1993).

[26] T. Nakanaga, F. Ito, and H. Takeo, Chem. Phys. Lett. **206**, 73 (1993).

[27] K. Kawaguchi, N. Sanechika, Y. Nishimura, R. Fujimori, T. N. Oka, Y. Hirahara, A. I. Jaman, and S. Civiš, Chem. Phys. Lett. **463**, 38 (2008).

[28] http://www.brukeroptics.com/opus.html.

[29] H. R. Pakhal, R. P. Lucht, and N. M. Laurendeau, Appl. Phys. B **90**, 15 (2008).

[30] S. Hafeez, N. M. Shaikh, B. Rashid, and M. A. Baig, J. Appl. Phys. **103**, 083117 (2008).

[31] V. N. Ochkin, *Spectroscopy of Low Temperature Plasma* (Wiley-VCH, Weinheim, 2009).

[32] M. B. Gaarde, R. Zerne, L. Caiyan, J. Zhankui, J. Larrson, and S. Svanberg, Phys. Rev. **50**, 209 (1994).

[33] H. Furusawa, T. Sakka, and Y. H. Ogata, J. Appl. Phys. **96**, 975 (2004).

[34] G. Simons, J. Chem. Phys. **60**, 645 (1974); I. Martin and G. Simons, *ibid.* **62**, 4799 (1975).

[35] P. G. Alcheev, V. E. Chernov, and B. A. Zon, J. Mol. Spectrosc. **211**, 71 (2002).

[36] N. L. Manakov, V. D. Ovsiannikov, and L. P. Rapoport, Phys. Rep. **141**, 319 (1986); N. L. Manakov, S. I. Marmo, and S. A. Sviridov, Zh. Eksp. Teor. Fiz. **132**, 796 (2007) [JETP **105**, 696 (2007)].

[37] I. S. Gradshteyn and I. M. Ryzhik, *Table of Integrals, Series, and Products* (Academic Press, Orlando, Florida, 2007).

[38] E. Yu. Il'inova and V. D. Ovsyannikov, Opt. Spektrosk. **105**, 709 (2008) [Opt. Spectrosc. **105**, 647 (2008)].

[39] V. E. Chernov, D. L. Dorofeev, I. Yu. Kretinin, and B. A. Zon, Phys. Rev. A **71**, 022505 (2005); E. V. Akindinova, V. E. Chernov, I. Yu. Kretinin, and B. A. Zon, *ibid.* **79**, 032506 (2009).

[40] L. A. Bureyeva and V. S. Lisitsa, *A Perturbed Atom* (Gordon and Beach, London, 2000).

[41] I. I. Sobelman, *Atomic Spectra and Radiative Transitions* (Springer-Verlag, Berlin, 1979).

[42] U. I. Safronova and W. R. Johnson, Phys. Rev. A **69**, 052511 (2004); U. I. Safronova (private communication).

[43] http://i-portal.nsu.ru/lemma.dll?db=GROTRIAN&int= ENGLISH_VIEW&class=CMAINVIEW&templ=MAIN.